

Electric field gradients in Zr_8Ni_{21} and Hf_8Ni_{21} intermetallic compounds; Results from perturbed angular correlation measurements and first-principles density functional theory

S.K. Dey¹, C.C. Dey^{1*}, S. Saha¹, J. Belošević-Čavor²

¹*Saha Institute of Nuclear Physics; I/AF, Bidhannagar, Kolkata - 700 064, India*

²*Institute of Nuclear Sciences Vinca, University of Belgrade, P. O. Box 522, 11001 Belgrade, Serbia*

Abstract

Numerous technological applications of Ni-based Zr and Hf intermetallic alloys promoted comprehensive studies in Zr_8Ni_{21} and Hf_8Ni_{21} by perturbed angular correlation (PAC) spectroscopy, which were not studied earlier until this report. The different phases produced in the samples have been identified by PAC and X-ray diffraction (XRD) measurements. Using ^{181}Hf probe, two non-equivalent Zr/Hf sites have been observed in both Zr_8Ni_{21} and Hf_8Ni_{21} compounds. From present PAC measurements in Zr_8Ni_{21} , a component due to the production of Zr_7Ni_{10} by eutectic reaction from the liquid metals is also observed. The phase Zr_7Ni_{10} , however, is not found from the XRD measurement. In Zr_8Ni_{21} , while the results do not change appreciably up to 973 K exhibit drastic changes at 1073 K. In Hf_8Ni_{21} , similar results for the two non-equivalent sites have been found but site fractions are in reverse order. In this alloy, a different contaminating phase, possibly due to $HfNi_3$, has been found from PAC measurements but is not found from XRD measurement. Density functional theory (DFT) based calculations of electric field gradient (EFG) and asymmetry parameter (η) at the sites of ^{181}Ta probe nucleus allowed us to assign the observed EFG fractions to the various lattice sites in $(\text{Zr/Hf})_8Ni_{21}$ compounds.

Keywords: A. intermetallics (miscellaneous) ; B. density functional theory ; C. mechanical alloying ; D. site occupancy ; E. ab initio calculations ; G. hydrogen storage

1. Introduction

Intermetallic binary alloys between the two elements of A (Hf/Zr/Ti) and B (Fe/Co/Ni) have many technological applications. They have properties like superior strength, corrosion resistance, hydrogen storage capacity, ferromagnetism and have applications in space craft industry, fuel cell etc. The Zr-Ni alloys, particularly, have excellent hydrogen storage properties and have applications in Ni-metal hydride (MH) rechargeable batteries as a negative electrode [1–3]. The gaseous hydrogen storage characteristics of four intermetallic compounds in the Zr-Ni system viz. Zr_9Ni_{11} , Zr_7Ni_{10} , Zr_8Ni_{21} and Zr_2Ni_7 were compared by Joubert et al. [1]. It was found that hydrogen storage capacities in hydrogen atoms per metal atom (H/M) for these four compounds are 0.93 (10 bar), 1.01 (10 bar), 0.34 (25 bar) and 0.29 (25 bar), respectively, at room temperature and the storage capacities for Zr_8Ni_{21} , Zr_2Ni_7 are completely reversible. The hydrogen reversible capacities for Zr_9Ni_{11} and Zr_7Ni_{10} , are 50% and 77%, respectively. The electrochemical properties of Zr_7Ni_{10} , Zr_9Ni_{11} and Zr_8Ni_{21} were studied by Ruiz et al. [2, 3] and Nei et al. [4, 5]. It was found [3] that

Zr_8Ni_{21} alloy had a better charge/discharge performance than Zr_7Ni_{10} and Zr_9Ni_{11} . A detailed review on the electrochemical properties of various compounds of Zr-Ni system for application of these materials in Ni-MH battery was reported by Young et al. [6]. The intermetallic compound $ZrNi_5$ was reported to have strong ferromagnetic properties by Drulis et al. [7]. A. Amamou [8] reported the electronic structure of various compounds in the Zr-Ni system, namely, Zr_2Ni , $ZrNi$, Zr_8Ni_{21} and $ZrNi_5$. Both magnetic and structural properties of the A_xB_y compounds can be studied experimentally by the nuclear technique of perturbed angular correlation (PAC), which uses a suitable radioactive isotope (usually ^{181}Hf) to characterize the materials. Using this technique, different intermetallic compounds in the Zr-Ni system have recently been studied, namely, $ZrNi_5$ [9, 10], Zr_2Ni_7 [11] and $ZrNi$ [12]. From the studies in $ZrNi_5$ system [9, 10], however, no magnetic interaction was found, in contradiction with the result from previous measurements by Drulis et al. [7].

Considering the important applications of Zr_8Ni_{21} , Zr_9Ni_{11} and Zr_7Ni_{10} as described above, we have done detailed PAC measurements in Zr_8Ni_{21} and Hf_8Ni_{21} intermetallic compounds. To the best of our knowledge, there is no measurement by PAC technique to characterize these materials. From previous studies [13], a pure single phase Zr_8Ni_{21} was not found to be produced by arc melting preparation. It was found [13] that Zr_8Ni_{21} was not formed congruently from the liquid. The

*corresponding author

Email addresses: skumar.dey@saha.ac.in (S.K. Dey¹), chandicharan.dey@saha.ac.in (C.C. Dey¹), satyajit.saha@saha.ac.in (S. Saha¹), cjece@vin.bg.ac.rs (J. Belošević-Čavor²)

Zr_2Ni_7 was first solidified from the liquid and then reacted with the remaining liquid to form Zr_8Ni_{21} alloy peritectically. The Zr_7Ni_{10} was formed eutectically from Zr_8Ni_{21} . The two other phases viz. Zr_2Ni_7 and Zr_7Ni_{10} were produced along with Zr_8Ni_{21} and were confirmed by scanning electron microscopy (SEM)/X-ray energy dispersive spectroscopy (EDS) compositional mapping and transmission electron microscopy (TEM) [13]. However, in the present report, we have studied both Zr_8Ni_{21} and Hf_8Ni_{21} to identify and characterize the different phases produced in these compounds. The secondary phases of small fractions that are produced along with the main phase can be determined quite accurately by this technique. The structural and compositional stability of Zr_8Ni_{21}/Hf_8Ni_{21} phases have been studied by temperature dependent PAC measurements.

The crystal structure of Zr_8Ni_{21} is known to be triclinic [14] and is isotropic to that of Hf_8Ni_{21} [15]. The lattice parameters of Zr_8Ni_{21} are $a=6.476$ Å, $b=8.064$ Å, $c=8.594$ Å, $\alpha=75.15^\circ$, $\beta=68.07^\circ$ and $\gamma=75.23^\circ$ as determined by X-ray diffraction analysis.

In the PAC technique [16–18], the angular correlation of a γ - γ cascade in a suitable probe nucleus is perturbed by the interaction of the probe nuclear moments with the electric field gradients/magnetic fields generated at the probe site due to surrounding charge distribution. The crystalline electric field gradient (EFG) and the internal magnetic field in a magnetic material can be determined by the PAC technique if the values of electromagnetic moments of the intermediate level of the probe nucleus are known. As the EFG depends on the charge distribution of the probe-nucleus environment, the temperature evolution of the lattice properties such as crystallographic structure, imperfections or defects, can be monitored by applying PAC technique over a wide temperature range. The combination of PAC measurements and ab-initio calculations proved to be an excellent method to study the structural phase stabilities and the localization of the impurities in the host lattice [19, 20]. In this paper, results of temperature dependent PAC measurements (77–1073 K) in both Zr_8Ni_{21} and Hf_8Ni_{21} as well as DFT calculations are reported. The calculated EFG values at the ^{181}Ta impurity sites are compared with experimental results.

2. Experimental details

The intermetallic compounds Zr_8Ni_{21} and Hf_8Ni_{21} were prepared by arc melting in an argon atmosphere. Stoichiometric amounts of high purity metals procured from M/S Alfa Aesar were used to prepare the samples. The purity of Zr (excluding Hf), Hf (excluding Zr) and Ni metals used were 99.2%, 99.95% and 99.98% respectively. For each sample, the constituent metals were alloyed homogeneously by repeated melting and then activated by remelting with a piece of ^{181}Hf metal. The ^{181}Hf metal was prepared by thermal neutron capture of natural ^{180}Hf metal in the Dhruba reactor, Mumbai using a flux $\sim 10^{13}/cm^2/s$. In both cases, shiny globule samples were formed and these were then sealed in evacuated quartz tubes for high temperature measurements. Different inactive samples of Zr_8Ni_{21} and Hf_8Ni_{21} were prepared similarly for XRD measurements. The

X-ray powder diffraction measurements have been carried out using the Rigaku X-ray diffractometer TTRAX-III and Cu K_α radiation.

The TDPAC technique measures the effect of perturbations of γ - γ angular correlation of the probe nucleus through the hyperfine interaction. In the present case, the probe ^{181}Hf substitutes the Zr atom in Zr_8Ni_{21} and is a constituent element in Hf_8Ni_{21} . In the β^- decay of ^{181}Hf , it populates the 615 keV excited level of ^{181}Ta which emits two successive γ rays, 133 and 482 keV passing through the 482 keV level with a half-life 10.8 ns and a spin angular momentum $I=5/2^+\hbar$ [21]. The angular correlation of the 133-482 keV cascade is perturbed by the extranuclear electric field gradients.

The perturbation function $G_2(t)$ for the electric quadrupole interaction in a polycrystalline material is given by [16]

$$G_2(t) = S_{20}(\eta) + \sum_{i=1}^3 S_{2i}(\eta) \cos(\omega_i t) \exp(-\delta\omega_i t) \exp\left[-\frac{-(\omega_i \tau_R)^2}{2}\right] \quad (1)$$

The frequencies ω_i correspond to transitions between the sub-levels of the intermediate state that arise due to nuclear quadrupole interaction (NQI). The parameter δ is the frequency distribution width (Lorentzian damping) which takes care of the chemical inhomogeneities in the sample and τ_R is the time resolution of the coincidence set up. Due to the presence of various non-equivalent sites, the perturbation factor $G_2(t)$ can generally be expressed as

$$G_2(t) = \sum_i f_i G_2^i(t), \quad (2)$$

where f_i is the site fraction of the i -th component. A fitting to eqn. (1) determines the maximum component V_{zz} of the electric field gradient from the measured quadrupole frequency ω_Q given by

$$\omega_Q = \frac{eQV_{zz}}{4I(2I-1)\hbar}, \quad (3)$$

where Q is the nuclear quadrupole moment of the 482 keV intermediate state (2.36 b). For an axially symmetric EFG ($\eta = 0$), ω_Q is related to ω_1 , ω_2 and ω_3 by

$$\omega_Q = \omega_1/6 = \omega_2/12 = \omega_3/18. \quad (4)$$

The principal EFG components obey the relations

$$V_{xx} + V_{yy} + V_{zz} = 0 \quad \text{and} \quad V_{zz} \geq V_{yy} \geq V_{xx}. \quad (5)$$

The EFG can therefore be designated by two parameters only viz. V_{zz} and η . The asymmetry parameter η is defined as

$$\eta = \frac{(V_{xx} - V_{yy})}{V_{zz}}, \quad 0 \leq \eta \leq 1. \quad (6)$$

The TDPAC spectrometer used for present measurements was a four detector $LaBr_3(Ce)$ - BaF_2 set up with crystal sizes 38×25.4 mm 2 for $LaBr_3(Ce)$ and 50.8×50.8 mm 2 for BaF_2 . The 133 keV γ -rays were selected in $LaBr_3(Ce)$ detectors. Standard slow-fast coincidence assemblies were employed to collect data at 180° and 90° . Typical prompt time resolution (FWHM) ~ 800

Table 1: Results of PAC measurements in Zr_8Ni_{21}

Temperature (K)	Component	ω_Q (Mrad/s)	η	$\delta(\%)$	$f(\%)$	Assignment
77	1	77.9(4)	0.80(1)	2(1)	55(3)	$Zr_8Ni_{21}^{(1)}$
	2	55.8(7)	0.68(2)	0	26(3)	Zr_7Ni_{10}
	3	101.5(9)	0.73(3)	0	18(3)	$Zr_8Ni_{21}^{(2)}$
298	1	75.8(2)	0.77(1)	1.1(6)	57(3)	$Zr_8Ni_{21}^{(1)}$
	2	54.4(4)	0.69(1)	0	27(3)	Zr_7Ni_{10}
	3	100.6(8)	0.72(3)	0	15(3)	$Zr_8Ni_{21}^{(2)}$
373	1	74.6(6)	0.75(2)	2(1)	53(3)	$Zr_8Ni_{21}^{(1)}$
	2	53(2)	0.71(3)	0	26(3)	Zr_7Ni_{10}
	3	97(2)	0.76(4)	0	21(3)	$Zr_8Ni_{21}^{(2)}$
473	1	73.1(5)	0.76(2)	2.4(8)	63(3)	$Zr_8Ni_{21}^{(1)}$
	2	52.1(7)	0.72(4)	0	37(3)	Zr_7Ni_{10}
573	1	71.8(3)	0.77(1)	2.5(6)	62(3)	$Zr_8Ni_{21}^{(1)}$
	2	52.9(5)	0.70(2)	0	38(3)	Zr_7Ni_{10}
673	1	70.1(6)	0.77(2)	4.5(8)	71(3)	$Zr_8Ni_{21}^{(1)}$
	2	50.8(4)	0.72(2)	0	29(3)	Zr_7Ni_{10}
773	1	68(1)	0.73(4)	4(2)	64(3)	$Zr_8Ni_{21}^{(1)}$
	2	48.4(9)	0.75(5)	0	36(3)	Zr_7Ni_{10}
873	1	67(3)	0.79(10)	8(4)	72(3)	$Zr_8Ni_{21}^{(1)}$
	2	48.8(8)	0.73(5)	0	28(3)	Zr_7Ni_{10}
973	1	65(2)	0.80(7)	7(3)	71(3)	$Zr_8Ni_{21}^{(1)}$
	2	47.3(6)	0.74(4)	0	29(3)	Zr_7Ni_{10}
1073	1	52.8(2)	0	1.3(7)	68(3)	Hf
	2	47(1)	0.71(9)	5(3)	32(3)	Zr_7Ni_{10}
298*	1	56.8(2)	0	4.0(9)	70(3)	Hf
	2	74.4(8)	0.79(1)	0	23(3)	$Zr_8Ni_{21}^{(1)}$
	3	74(2)	0.21(10)	0	7(3)	Zr_2Ni_7

* after measurement at 1073 K

ps was obtained for the ^{181}Hf energy window settings. The perturbation function $G_2(t)$ is found from the four coincidence spectra at 180° and 90° . Details of the experimental set up and data analysis can be found in reference [22].

3. PAC results

3.1 Zr_8Ni_{21}

The XRD powder pattern of Zr_8Ni_{21} sample is shown in figure 1. The X-ray analysis has been carried out using the known crystallographic data of Zr_8Ni_{21} [14]. The XRD spectrum shows no other peaks except for Zr_8Ni_{21} and this sample is, therefore, found to be produced in an almost pure single component phase. If any small contaminating phases like Zr_7Ni_{10} or Zr_2Ni_7 are produced, it is not observed from the XRD powder pattern.

The TDPAC spectra of ^{181}Ta in the as prepared sample of Zr_8Ni_{21} are shown in figure 2. From PAC measurements, three frequency components at room temperature have been obtained (Table 1). The components 1 and 3 have been attributed to Zr_8Ni_{21} by comparing with our PAC results in Hf_8Ni_{21} and results from ab-initio calculations by density functional theory (discussed later). The component 2 has been attributed to Zr_7Ni_{10} . This follows from the previous X-ray EDS and

Table 2: Results of PAC measurements in Hf_8Ni_{21}

Temperature (K)	Component	ω_Q (Mrad/s)	η	$\delta(\%)$	$f(\%)$	Assignment
77	1	99.3(3)	0.62(1)	2.5(5)	56(3)	$Hf_8Ni_{21}^{(2)}$
	2	80.7(9)	0.73(3)	0	16(3)	$Hf_8Ni_{21}^{(1)}$
	3	32.3(6)	0	0	19(3)	$HfNi_3$
	4	52(2)	0	0	8(3)	Hf
298	1	97.3(3)	0.63(1)	2.3(4)	63(3)	$Hf_8Ni_{21}^{(2)}$
	2	79.1(7)	0.75(2)	0	21(3)	$Hf_8Ni_{21}^{(1)}$
	3	31(1)	0	0	10(3)	$HfNi_3$
	4	50(2)	0	0	5(3)	Hf
373	1	95.3(6)	0.61(2)	2(1)	66(3)	$Hf_8Ni_{21}^{(2)}$
	2	76(3)	0.74(1)	0	13(3)	$Hf_8Ni_{21}^{(1)}$
	3	31(2)	0	0	15(3)	$HfNi_3$
	4	50(4)	0	0	7(3)	Hf
473	1	95.5(5)	0.62(1)	3(fixed)	61(3)	$Hf_8Ni_{21}^{(2)}$
	2	77(1)	0.74(3)	0	16(3)	$Hf_8Ni_{21}^{(1)}$
	3	28.6(7)	0	0	19(3)	$HfNi_3$
	4	45(4)	0	0	4(3)	Hf
573	1	92.1(3)	0.60(1)	3.2(5)	61(3)	$Hf_8Ni_{21}^{(2)}$
	2	75(1)	0.71(3)	0	14(3)	$Hf_8Ni_{21}^{(1)}$
	3	27.9(5)	0	0	19(3)	$HfNi_3$
	4	46(2)	0	0	5(3)	Hf
673	1	87.7(5)	0.61(1)	3(1)	59(3)	$Hf_8Ni_{21}^{(2)}$
	2	73(1)	0.66(4)	0	17(3)	$Hf_8Ni_{21}^{(1)}$
	3	27.5(9)	0	0	16(3)	$HfNi_3$
	4	43(2)	0	0	8(3)	Hf
773	1	89.1(6)	0.56(1)	6(1)	74(3)	$Hf_8Ni_{21}^{(2)}$
	2	73(2)	0.69(6)	0	8(3)	$Hf_8Ni_{21}^{(1)}$
	3	27.7(5)	0	0	18(3)	$HfNi_3$
	4	26.8(7)	0.57(2)	7(1)	82(3)	$Hf_8Ni_{21}^{(2)}$
873	1	84.2(5)	0.58(1)	7(1)	80(3)	$Hf_8Ni_{21}^{(2)}$
	2	27.0(5)	0	0	20(3)	$HfNi_3$
	1	82.7(7)	0.57(2)	7(1)	82(3)	$Hf_8Ni_{21}^{(2)}$
973	1	26.8(7)	0	0	18(3)	$HfNi_3$
	2	26.5(4)	0	5(1)	70(3)	$HfNi_3$
	3	78.7(6)	0.57(2)	0	15(3)	$Hf_8Ni_{21}^{(2)}$
1073	1	63.3(9)	0.23(8)	0	15(3)	Hf_2Ni_7
	2	30.2(4)	0	9(2)	62(3)	$HfNi_3$
	3	50.8(4)	0	0	25(3)	Hf
298*	1	70.0(8)	0	0	12(3)	Hf_2Ni_7

* after measurement at 1073 K

SEM/TEM results reported by Shen et al. [13]. The characteristic frequency and η for this component are distinctly different than those found in Zr_2Ni_7 [11]. Moreover, assignment of this component can be supported from our PAC measurements in Zr_7Ni_{10} [23] where, a component similar to this was found. It is found that three frequency components are required to fit the spectra in the temperature range 77-373 K with no appreciable change in parameters (Table 1). Variations of ω_Q , η and site fraction (f) with temperature for the two components of Zr_8Ni_{21} are shown in figure 3.

At 473 K, however, the PAC spectrum gives two components. The component $Zr_8Ni_{21}^{(2)}$ does not exist at this temperature. In the temperature range 473-973 K, no appreciable changes in results are observed (Table 1). But at 1073 K, a drastic change in PAC spectrum is found. At this temperature, the predominant component ($\sim 68\%$) produces a sharp decrease in quadrupole frequency and asymmetry parameter shows a value equal to

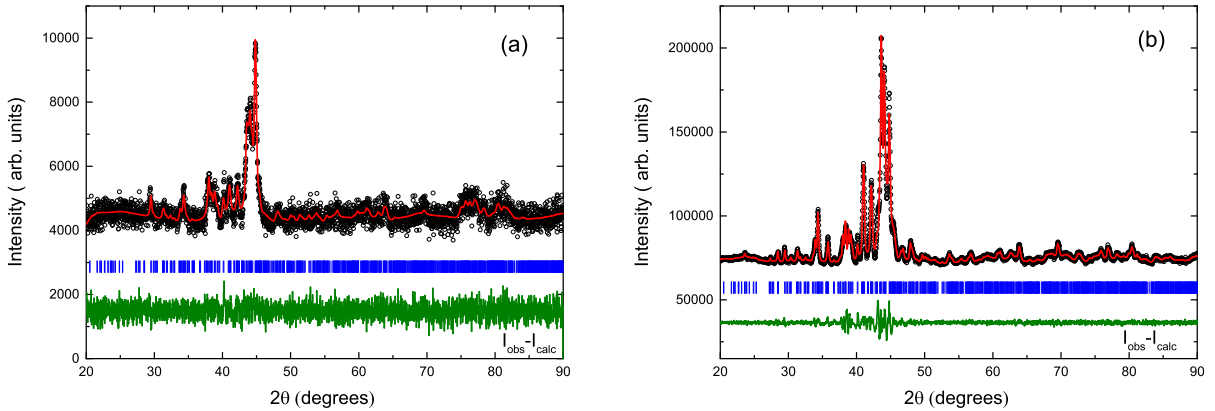


Figure 1: The XRD spectra in $\text{Zr}_8\text{Ni}_{21}$. Figure (a) shows the spectrum in as prepared sample and figure (b) shows the spectrum in a sample annealed at 1073 K for two days. The line represents the fit to the measured data, the vertical bars denote the Bragg angles and the bottom line shows the difference between the observed and the fitted pattern.

zero. This possibly indicates a change in local environment of the probe. The component due to $\text{Zr}_7\text{Ni}_{10}$, on the other hand, remains almost unchanged.

To understand the change in PAC spectrum at 1073 K, we have repeated the PAC measurement at room temperature. In the re-measured spectrum at 298 K, the predominant component (~70%) produces values of $\omega_Q \sim 57$ Mrad/s, $\eta \sim 0$. At the remeasured room temperature, it is found that the major component of $\text{Zr}_8\text{Ni}_{21}$ found initially at room temperature reappears with a much smaller fraction (Table 1). One additional new component is observed with a very small fraction which can be assigned to Zr_2Ni_7 by comparing with the previous result in Zr_2Ni_7 [11]. From SEM/X-ray EDS measurement [13] also, Zr_2Ni_7 was found in a sample of $\text{Zr}_8\text{Ni}_{21}$ annealed at 1233 K.

We have performed XRD measurement in a sample of $\text{Zr}_8\text{Ni}_{21}$ annealed at 1073 K for two days. The XRD spectrum (Fig. 1) shows peaks mainly due to $\text{Zr}_8\text{Ni}_{21}$. This indicates that no major structural or compositional phase transformation occurs at 1073 K.

Possible explanation for the predominant component observed at 1073 K and subsequently at room temperature is the following. Probably, the probe ^{181}Hf was not settled well at the position of $\text{Zr}_8\text{Ni}_{21}$ and at 1073 K, these probe atoms got enough energy to go out from the position. The major component is, therefore, observed due to the Hf probe itself.

The electric field gradients in metal and intermetallic compound are found to vary with temperature following T or $T^{3/2}$ relationship [24]. In $\text{Zr}_8\text{Ni}_{21}$, it is found that quadrupole frequencies vary with $T^{3/2}$ for both components. For the predominant site $\text{Zr}_8\text{Ni}_{21}^{(1)}$ (present up to 973 K), the results are fitted by

$$\omega_Q(T) = \omega_Q(0)[1 - \beta T^{3/2}]. \quad (7)$$

A least squares fitting gives results $\omega_Q(0) = 78.2(1)$ Mrad/s and $\beta = 5.9(1) \times 10^{-6} \text{ K}^{-3/2}$.

3.2 $\text{Hf}_8\text{Ni}_{21}$

The powder XRD pattern of $\text{Hf}_8\text{Ni}_{21}$ is shown in figure 4. The spectrum is fitted using the known crystallographic data

of $\text{Hf}_8\text{Ni}_{21}$ [15]. The X-ray analysis shows that there are no other peaks except for $\text{Hf}_8\text{Ni}_{21}$ and this sample is also found to be produced in an almost pure single component phase. No contaminating phase is obtained from the XRD powder pattern.

The TDPAC spectra of ^{181}Ta in $\text{Hf}_8\text{Ni}_{21}$ are shown in figure 5. The spectrum at room temperature produces four interaction frequencies. The first two components at room temperature with site fractions 63% and 21% (Table 2) are found to be quite similar to the components found in $\text{Zr}_8\text{Ni}_{21}$. The third weak component can possibly be attributed to HfNi_3 produced along with $\text{Hf}_8\text{Ni}_{21}$. L. Bsenko [25] reported the decomposition of $\text{Hf}_8\text{Ni}_{21}$ to HfNi_3 eutectoidally at $1175 \pm 10^\circ\text{C}$. This component has been found in the whole temperature range. The assignment of HfNi_3 in $\text{Hf}_8\text{Ni}_{21}$ can be supported also from our PAC measurements in HfNi_3 [26] where a similar component to this was found. A very weak component (~5%) found at room temperature can be attributed to Hf probe which is not settled in the compound. From our temperature dependent PAC measurements, it is found that all four components exist in the temperature range 77-673 K. The component 4 is not observed at 773 K and the minor site of $\text{Hf}_8\text{Ni}_{21}$ ($\text{Hf}_8\text{Ni}_{21}^{(1)}$) disappears at 873 K. A drastic change in PAC spectrum is observed at 1073 K where the tentatively assigned HfNi_3 component suddenly increases at the expense of $\text{Hf}_8\text{Ni}_{21}$ (Table 2). The component due to $\text{Hf}_8\text{Ni}_{21}$ reduces to only 15%. At this temperature, a new frequency component (component 3) is observed which probably can be attributed to Hf_2Ni_7 by comparing its values with the results reported in the analogous compound Zr_2Ni_7 [11].

After measurement at 1073 K, a re-measurement at 298 K is carried out. In the re-measurement, HfNi_3 is found to be predominant (~62%) which appeared as a minor fraction (~10%) initially at room temperature. Here, no component due to $\text{Hf}_8\text{Ni}_{21}$ is observed. A small component fraction of $\text{Hf}_8\text{Ni}_{21}$ found at 1073 K and absence of this fraction at remeasured room temperature indicates that $\text{Hf}_8\text{Ni}_{21}$ is not a stable phase approximately above 1000 K. It is found also that, the component due to Hf probe atom re-appears at this temperature with a higher component fraction (~25%). The quadrupole frequency and asymmetry parameter for this component ($\omega_Q = 50.8$

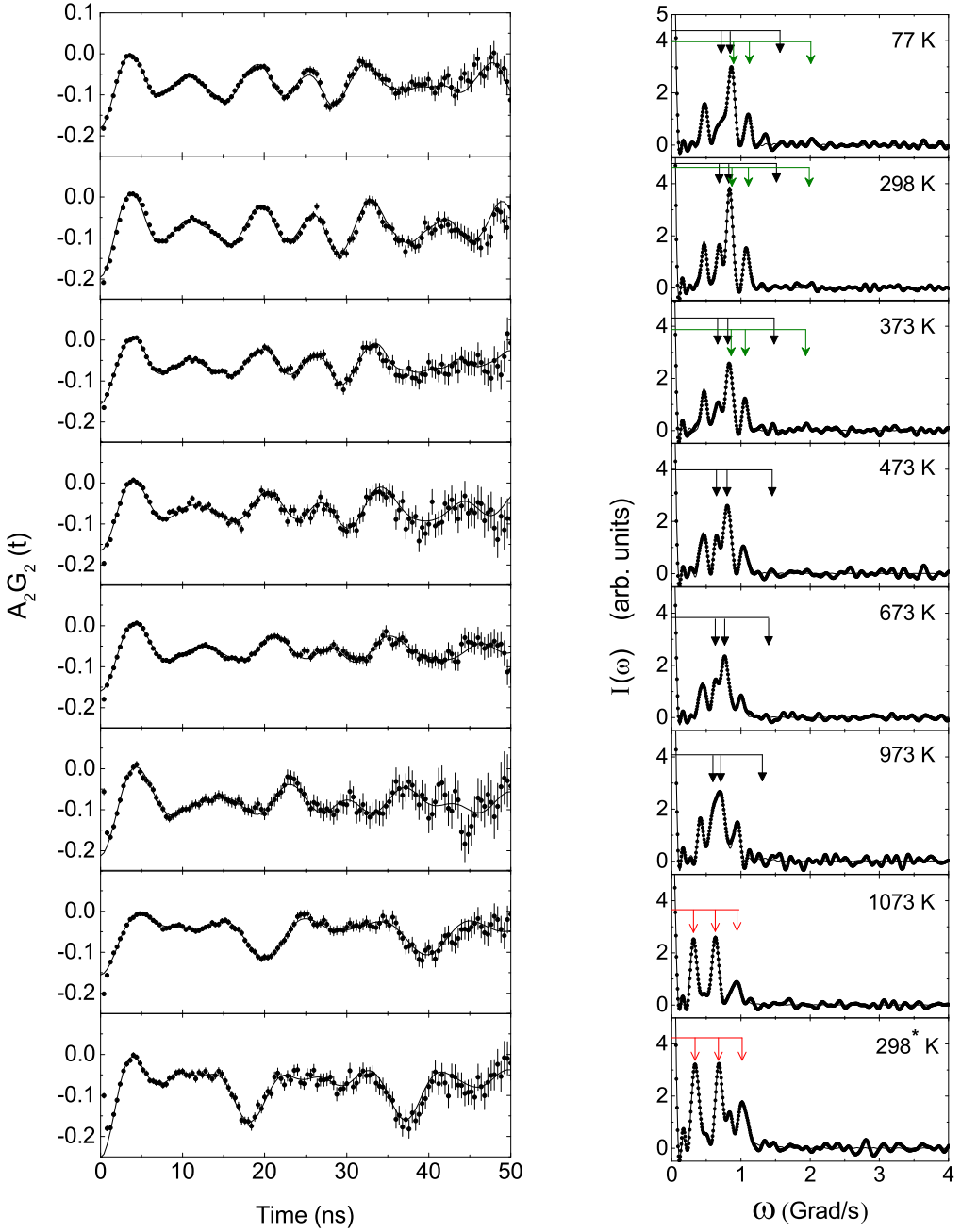


Figure 2: TDPAC spectra in $\text{Zr}_8\text{Ni}_{21}$ at different temperatures. Left panel shows the time spectra and the right panel shows the corresponding Fourier transforms. The PAC spectrum designated by 298^* K is taken after the measurement at 1073 K. The two sets of arrows in each Fourier spectrum (up to 373 K) correspond to two non-equivalent ^{181}Ta sites in $\text{Zr}_8\text{Ni}_{21}$. Arrows shown in the Fourier spectra at 1073 and 298^* K correspond to Hf.

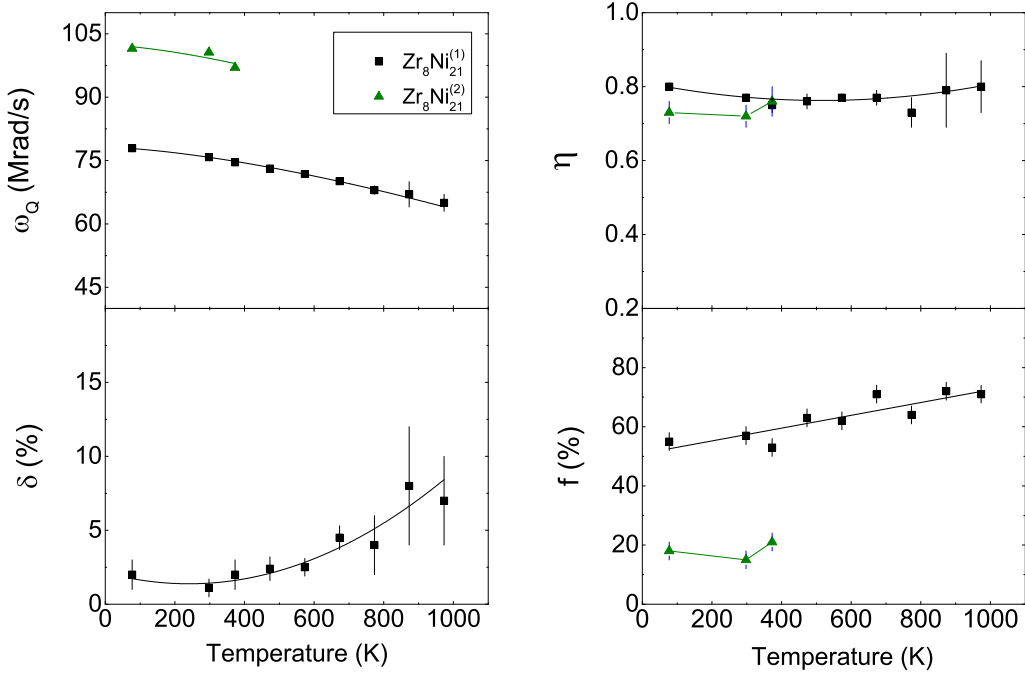


Figure 3: Variations of quadrupole frequency (ω_Q), asymmetry parameter (η) and site fraction $f(\%)$ with temperature for the two non-equivalent ^{181}Ta sites in $\text{Zr}_8\text{Ni}_{21}$. Variation of δ is shown for the component $\text{Zr}_8\text{Ni}_{21}^{(1)}$.

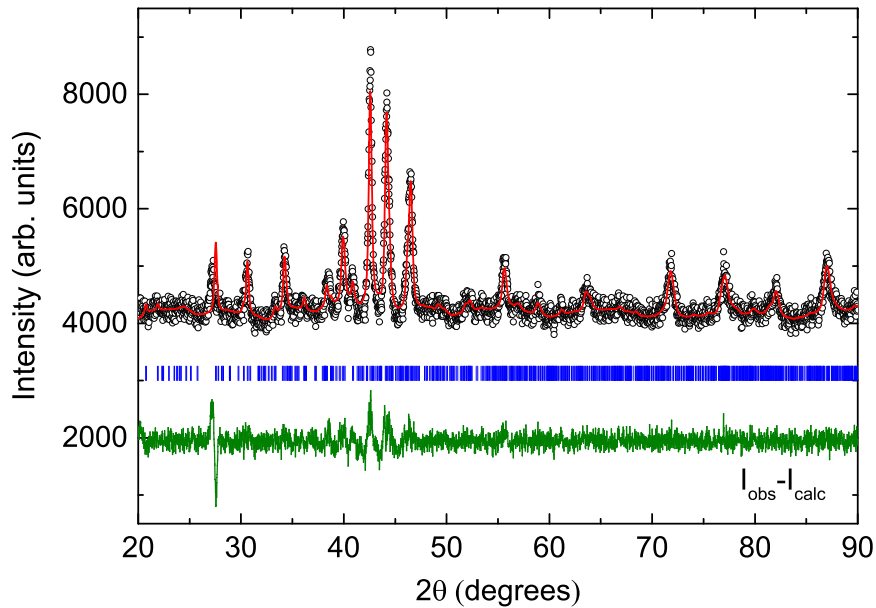


Figure 4: The background subtracted XRD powder pattern in $\text{Hf}_8\text{Ni}_{21}$. The line represents the fit to the measured data, the vertical bars denote the Bragg angles and the bottom line shows the difference between the observed and the fitted pattern.

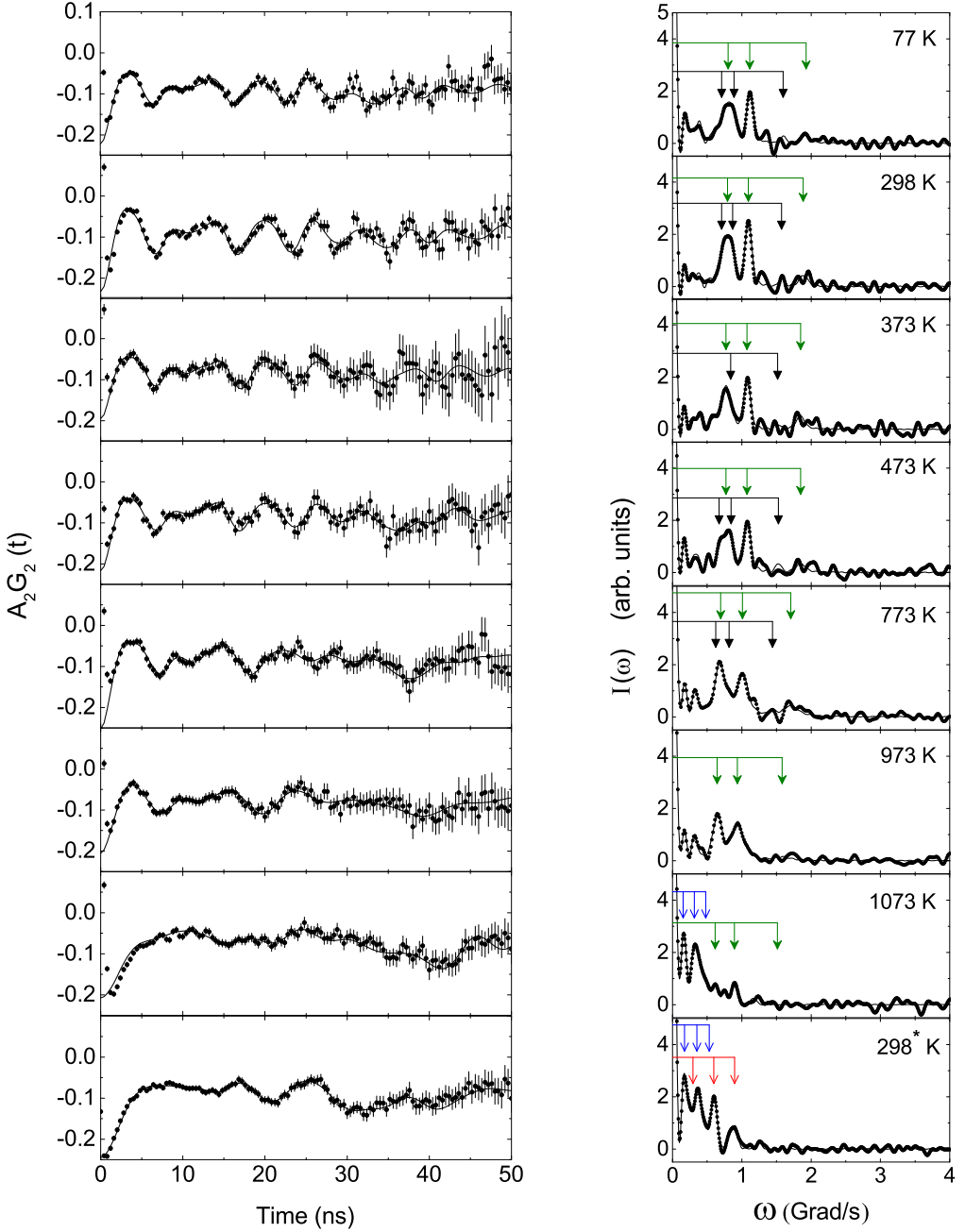


Figure 5: TDPAC spectra in $\text{Hf}_8\text{Ni}_{21}$ at different temperatures. Left panel shows the time spectra and the right panel shows the corresponding Fourier transforms. The PAC spectrum designated by 298^* K is taken after the measurement at 1073 K. The two sets of arrows in each Fourier spectrum (up to 773 K) correspond to two different ^{181}Ta sites in $\text{Hf}_8\text{Ni}_{21}$. Two sets of arrows in the Fourier spectrum at 298^* K correspond to HfNi_3 and Hf .

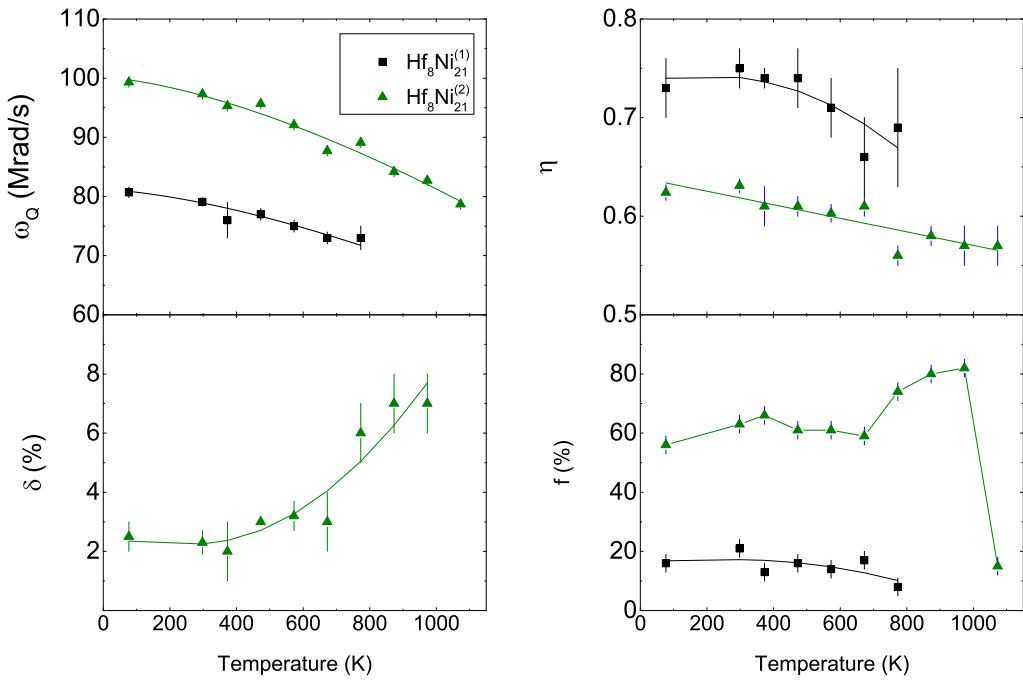


Figure 6: Variations of quadrupole frequency (ω_Q), asymmetry parameter (η) and site fraction $f(\%)$ with temperature for the two non-equivalent ^{181}Ta sites in $\text{Hf}_8\text{Ni}_{21}$. Variations of δ is shown for the site $\text{Hf}_8\text{Ni}_{21}^{(2)}$.

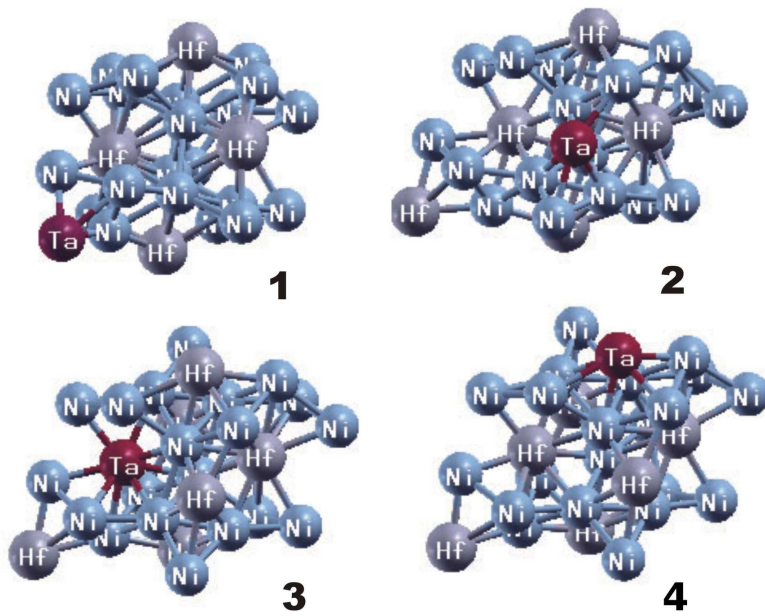


Figure 7: Models of four types of cells used in this study

Table 3: Calculated EFG values in units of 10^{21} V/m² and asymmetry parameters

Probe	Lattice Site	EFG	η	Measured EFG extrapolated to 0 K	Measured η at 77 K
no probe (pure compound) Zr_8Ni_{21}	Zr(1) 2i 0.0691(4) 0.9052(3) 0.3147(3)	-3.5	0.82		
	Zr(2) 2i 0.2460(4) 0.4364(3) 0.0344(3)	-4.1	0.85		
	Zr(3) 2i 0.2462(4) 0.5604(3) 0.6070(3)	-5.0	0.88		
	Zr(4) 2i 0.5685(4) 0.0374(3) 0.2475(3)	-4.7	0.74		
^{181}Ta in Zr_8Ni_{21}	Zr(1) 2i 0.0691(4) 0.9052(3) 0.3147(3)	8.8	0.91	8.7(2)	0.80(1)
	Zr(2) 2i 0.2460(4) 0.4364(3) 0.0344(3)	-11.4	0.55		
	Zr(3) 2i 0.2462(4) 0.5604(3) 0.6070(3)	-12.5	0.78	11.4(1)	0.73(3)
	Zr(4) 2i 0.5685(4) 0.0374(3) 0.2475(3)	-12.3	0.56		
no probe (pure compound) Hf_8Ni_{21}	Hf(1) 2i 0.2487(3) 0.0620(3) 0.1072(3)	-11.5	0.75		
	Hf(2) 2i 0.0688(3) 0.4040(2) 0.8150(2)	-8.1	0.91		
	Hf(3) 2i 0.4312(3) 0.4633(3) 0.2543(3)	-10.8	0.69		
	Hf(4) 2i 0.2452(3) 0.9375(3) 0.5340(2)	-10.2	0.64		
^{181}Ta in Hf_8Ni_{21}	Hf(1) 2i 0.2487(3) 0.0620(3) 0.1072(3)	-13.3	0.71		
	Hf(2) 2i 0.0688(3) 0.4040(2) 0.8150(2)	9.6	0.88	9.1(1)	0.73(3)
	Hf(3) 2i 0.4312(3) 0.4633(3) 0.2543(3)	-12.5	0.60		
	Hf(4) 2i 0.2452(3) 0.9375(3) 0.5340(2)	-11.8	0.51	11.2(2)	0.62(1)

$Mrad/s$, $\eta=0$) are very much similar to the values in a Hf metal [27].

Variations of ω_Q , η , δ and site fraction (f) for different components observed in Hf_8Ni_{21} in the temperature range 77-1073 K are shown in figure 6. In Hf_8Ni_{21} also, the quadrupole frequencies for the two sites show $T^{3/2}$ temperature dependent behaviors. A least squares fitting (eqn. 7) for the predominant site (present up to 1073 K) gives values of $\omega_Q(0)=100.1(5)$ $Mrad/s$, $\beta=6.0(3)\times 10^{-6} K^{-3/2}$. For the minor site (present up to 773 K), the fitted results are found to be $\omega_Q(0)=81.2(4)$ $Mrad/s$, $\beta=5.4(3)\times 10^{-6} K^{-3/2}$. Similar values of β for both components indicate similar temperature dependent behaviors for the two sites. Also, the values of β are quite similar to the value of β in Zr_8Ni_{21} for the site $Zr_8Ni_{21}^{(1)}$.

4. DFT calculation

The first-principles density functional theory (DFT) calculations were performed to compare with the experimental results and to dispel the doubts existing in the interpretation of the experimental data. All the calculations were done with WIEN2k simulation package [28], based on the full potential (linearized) augmented plane waves method (FP (L)APW). Electronic exchange-correlation energy was treated with generalized gradient approximation (GGA) parametrized by Perdew-Burke-Ernzerhof (PBE) [29]. In our calculations the muffin-tin radii for Zr, Ni and Ta (Hf) were 2.3, 2.2 and 2.4 a. u., respectively. The cut-off parameter $R_{mt}K_{max}$ for limiting the number of plane waves was set to 7.0, where R_{mt} is the smallest value of all atomic sphere radii and K_{max} is the largest reciprocal lattice vector used in the plane wave expansion.

The Brillouin zone integrations within the self-consistency cycles were performed via a tetrahedron method [30], using 18 k points in the irreducible wedge of the Brillouin zone ($4\times 3\times 3$ mesh). The atomic positions were relaxed according to Hellmann-Feynman forces calculated at the end of each

self-consistent cycle, with the force minimization criterion 2 mRy/a.u.. In our calculations the self-consistency was achieved by demanding the convergence of the integrated charge difference between last two iterations to be smaller than 10^{-5} . Both Zr_8Ni_{21} and Hf_8Ni_{21} crystallize in the triclinic P1 type structure, which possesses 15 non-equivalent crystallographic positions [14, 15], 4 for Zr (Hf) atoms and 11 for Ni atoms. All Zr (Hf) non-equivalent positions have the same point group symmetry 2i and 3 Zr and 12 Ni atoms as nearest neighbors, except Zr(3), which has 2 Hf and 13 Ni. Each of the four non-equivalent Zr (Hf) atoms in the unit cell, stated in references [14, 15] was replaced by Ta subsequently (figure 7, [31]) preserving the point group symmetry around original atom and then electric field gradients at thus created Ta positions were calculated using the method developed in reference [32].

The usual convention is to designate the largest component of the EFG tensor as V_{zz} . The asymmetry parameter η is then given by $\eta = (V_{xx} - V_{yy})/V_{zz}$, where $V_{zz} \geq V_{yy} \geq V_{xx}$. The calculated EFGs in the pure compounds as well as at Ta probe positions in the investigated compounds are given in Table 3.

It can be observed that there is not much difference in the EFG values for four non-equivalent Zr positions in the pure Zr_8Ni_{21} compound. EFG is the smallest at Zr1 and the largest at Zr3. This trend is preserved also for the electric field gradients calculated at the corresponding Ta positions, but the EFGs are now about 2.5 times larger. In the pure Hf_8Ni_{21} compound, EFG values are about doubled, as compared to the corresponding ones for Zr_8Ni_{21} , but the η values are similar. Here, also, introduction of Ta atom at one of the non-equivalent Hf sites, leads to increased EFG values.

5. Discussion

In the temperature range 77-373 K, Zr_8Ni_{21} PAC spectra consist of three frequency components. A uniform conversion from the measured quadrupole frequencies to the EFGs is achieved

using the value of 2.36×10^{-24} cm 2 [33] for the quadrupole moment of ^{181}Hf . By comparing the measured results for the EFGs and asymmetry parameters with the calculated ones, components 1 and 3 (Table 1) are attributed to the two non-equivalent Zr sites in $\text{Zr}_8\text{Ni}_{21}$. The measured values of EFGs (8.7×10^{21} V/m 2 and 11.3×10^{21} V/m 2) and η (0.80 and 0.73) at 77 K are in excellent agreement with the calculated values for the two Zr sites in $\text{Zr}_8\text{Ni}_{21}$. However, as Ta doped $\text{Zr}_8\text{Ni}_{21}$ has four non-equivalent crystallographic positions with similar EFG and asymmetry parameter (Table 3), in order to explain preferential site occupation, we performed ab initio total energy calculations for Ta doped $\text{Zr}_8\text{Ni}_{21}$ and found that the configuration obtained when Ta replaces Zr(3) position has the lowest formation energy, about 0.013 eV lower than the structure when Ta is at Zr(1) position. The formation energies of the remaining two configurations are about 0.1 eV higher.

At 1073 K, there is a drastic change of PAC spectrum in $\text{Zr}_8\text{Ni}_{21}$. At this temperature, EFG for the predominant component produces a zero value of η . A similar change in ^{181}Ta PAC spectra with increasing temperature above 650 K was observed in TiPd_2 compound [34] and was explained with the shift of Ta atom from Ti to Pd lattice site [34, 35], but in our case, DFT calculations excluded that possibility, as all of the non-equivalent Ni sites in $\text{Zr}_8\text{Ni}_{21}$ has η which differs from zero. We find a resemblance of EFG and η for the component 1 in $\text{Zr}_8\text{Ni}_{21}$ at re-measured room temperature and component 4 in $\text{Hf}_8\text{Ni}_{21}$ with the calculated values for Ta in pure Hf metal (6.7×10^{21} V/m 2 and $\eta = 0$).

The PAC spectrum for $\text{Hf}_8\text{Ni}_{21}$ at room temperature consists of four components. The first two components with the EFG values 11.1×10^{21} V/m 2 and 9.0×10^{21} V/m 2 and the corresponding asymmetry parameters 0.62 and 0.73 (at 77 K) obviously correspond to the two different Hf positions in $\text{Hf}_8\text{Ni}_{21}$ (Table 3). The measured results show that quadrupole frequencies for the two corresponding sites in $\text{Zr}_8\text{Ni}_{21}$ and $\text{Hf}_8\text{Ni}_{21}$ vary in similar manner with temperature.

6. Conclusion

We have presented the time differential perturbed angular correlations measurements and DFT calculations to determine the electric field gradients in $\text{Zr}_8\text{Ni}_{21}$ and $\text{Hf}_8\text{Ni}_{21}$ intermetallic compounds. Our results indicate that during the preparation of $\text{Zr}_8\text{Ni}_{21}$ by arc melting, other phases like $\text{Zr}_7\text{Ni}_{10}$ can also be formed. The same goes for $\text{Hf}_8\text{Ni}_{21}$, in which HfNi_3 compound was detected. In both $\text{Zr}_8\text{Ni}_{21}$ and $\text{Hf}_8\text{Ni}_{21}$, EFGs for two non-equivalent sites of Zr/Hf, vary following $T^{3/2}$ relationship with temperature. Temperature dependent PAC measurement show that $\text{Hf}_8\text{Ni}_{21}$ is probably not a stable phase above 1000 K.

Acknowledgement

One of the authors (C.C. Dey) gratefully acknowledges the help of Prof. Dr. T. Butz, University of Leipzig, Germany in data analysis. The authors acknowledge with thanks A. Karma-hapatra and S. Pakhira of Saha Institute of Nuclear Physics, Kolkata for their helps in XRD measurements and data analysis. The present work is supported by the Department of Atomic Energy, Government of India through the Grant no. 12-R&D-SIN-5.02-0102. Finally, J. Belošević-Čavor acknowledges support by The Ministry of Education, Science and Technological Department of the Republic of Serbia through the project no. 171001.

References

- [1] J.M. Joubert, M. Latroche, A. Percheron-Guègan, *J. Alloys Compd.* 231 (1995) 494.
- [2] F.C. Ruiz, E.B. Castro, S.G. Real, H.A. Peretti, A. Visintin, W.E. Triaca, *Int. J. Hydrogen Energy*, 33 (2008) 3576.
- [3] F. C. Ruiz, E. B. Castro, H. A. Peretti, A. Visintin, *Int. J. Hydrogen Energy* 35 (2010) 9879.
- [4] J. Nei, K. Young, R. Regmi, G. Lawes, S.O. Salley, K.Y.S. Ng, *Int. J. Hydrogen Energy* 37 (2012) 16042.
- [5] J. Nei, K. Young, S. O. Salley, K. Y. S. Ng, *J. Alloys Compd.* 516 (2012) 144.
- [6] Kwo-hsiung Young, Jean Nei, *Materials* 6 (2013) 4574.
- [7] H. Drulis, W. Iwasieczko, V. Zaremba, *J. Mag. Mag. Materails* 256 (2003) 139.
- [8] A. Amamou, *Solid State commun.* 37 (1981) 7.
- [9] C. C. Dey, *J. Mag. Mag. Materials* 342 (2013) 87.
- [10] P.R.J. Silva, H. Saitovitch, J.T. Cavalcante, M. Forker, *J. Mag. Mag. Materials* 322 (2010) 1841.
- [11] C. C. Dey and S. K. Srivastava, *Physica B* 427 (2013) 126.
- [12] C. C. Dey, Rakesh Das and S. K. Srivastava, *J. Phys. Chem. Solids* 82 (2015) 10.
- [13] Haoting Shen, Leonid A. Bendersky, Kwo Young, Jean Nei, *Materials* 8 (2015) 4618.
- [14] J. M. Joubert, R. cerný, K. Yvon, Z. Kristallogr. New Cryst. Struct. 213 (1998) 227.
- [15] L. Bsenko, *Acta. Cryst. B* 34 (1978) 3204.
- [16] G. Schatz, A. Weidinger, Nuclear condensed matter physics, Nuclear Methods and Application, John Wiley and Sons, Chichester, New York, Brisbane, Toronto, Singapore, 1996, p. 63 (chapter 5).
- [17] G. L. Catchen, *Mater. Res. Soc. Bull.* XX (7), 37 (1995).
- [18] M. Zacate and H. Jaeger, *Defect Diffus. Forum* 311 (2011) 3.
- [19] L. A. Errico, H. M. Petrilli, L. A. Terrazos, A. Kulińska, P. Wodniecki, K. P. Lieb, M. Uhrmacher, J. Belosevic-Cavor, V. Koteski, *J. Phys. Condens. Matter* 22 (2010) 215501.
- [20] P. Wodniecki, A. Kulińska, B. Wodniecka, S. Cottenier, H. M. Petrilli, M. Uhrmacher, K. P. Lieb, *Europhysics Letters* 77 (2007) 43001.
- [21] R. B. Firestone, V. S. Shirley (Eds.), Table of Isotopes, 8th ed., John Wiley and Sons, New York, 1996.
- [22] C. C. Dey, *Pramana* 70 (2008) 835.
- [23] S. K. Dey, C. C. Dey, S. Saha, J. Belošević-Čavor (to be published).
- [24] W. Witthuhn and E. Engel, in Hyperfine Interactions of Radioactive Nuclei, Ed. by J. Christiansen (Springer-Verlag Berlin Heidelberg New York Tokyo, 1983) P. 205.
- [25] Lars Bsenko, *J. Less Common Met.* 63 (1979) 171.
- [26] S. K. Dey, C. C. Dey, S. Saha, J. Belošević-Čavor (to be published).
- [27] S. K. Dey, C. C. Dey, S. Saha, *J. Phys. Chem. Solids* 95 (2016) 98.
- [28] P. Blaha, K. Schwarz, G. K. H. Madsen, D. Kvasnicka, J. Luitz, WIEN2k an Augmented Plane Wave Plus Local Orbitals Program for Calculating Crystal Properties, Vienna University of Technology, Vienna, Austria, 2001.
- [29] J. P. Perdew, K. Burke, M. Ernzerhof, *Phys. Rev. Lett.* 77 (1996) 3865.
- [30] P. E. Blochl, O. Jepsen, O. K. Andersen, *Phys. Rev. B* 49 (1994) 16223.

- [31] A. Kokalj, J. Mol. Graphics Modelling 17 (1999) 176.
- [32] P. Blaha, K. Schwarz, Phys. Rev. Lett. 54 (1985) 1192.
- [33] T. Butz, A. Lerf, Phys. Lett. A 97 (1983) 217.
- [34] P. Wodniecki, B. Wodniecka, A. Kulińska, M. Uhrmacher, K. P. Lieb, Journal of Alloys and Compounds 385 (2004) 53.
- [35] J. Belošević-Čavor, V. Koteski, J. Radaković, Solid State Communications, 152 (2012) 1072.